Detection and Localization of Open-Phase Fault in Three-Phase Induction Motor Drives Using Second Order Rotational Park Transformation

Ali Hajary, Reza Kianinezhad, S.Gh Seifossadat, S.S Mortazavi, and Alireza Saffarian

***Abstract*—The open-phase fault in vector-controlled drives is known as one of the most prevalent failures that require immediate detection. It is still challenging to develop a trustable fault diagnosis scheme at light load, transients, and low-speed regions. This paper presents a novel open-phase fault diagnosis strategy for three-phase induction motor drives over the entire speed range and for different load conditions. By taking advantage of the second-order rotational park transformation (SORP), new fault indices are proposed to identify the open-phase location without using any additional sensors or electric equipment. Comparing with root-mean-square (RMS) calculation-based methods, the proposed method detects the fault at least twice faster, with minimal system resources. The presented scheme may be implemented simply and is robust against the operating point changes. Proof of the proposed fault detection and localization method has been shown through experimental tests on a 250-W three-phase induction machine which is controlled by TI-DSP F28335.**

***Index Terms*—Fault diagnosis, open-phase fault detection, second-order rotational park transformation, three-phase induction motor.**

I. Introduction

THREE-PHASE induction motor drives have become one of the main devices in various high-performance industrial applications such as hybrid and electric vehicles, automotive powertrains, oil pumps, and renewable energy conversion systems [1]–[3]. For these applications, fast and secure fault detection becomes essential to prevent damage to the motor drive system and guarantee high-reliability levels. On the other hand, in order to achieve a fault-tolerant control, the machine failures have to be immediately and effectively detected [3]–[6].

For implementing advanced speed control algorithms, highly efficient semiconductor switches are used to generate pulsewidth modulation (PWM) voltages. Hence, the reliability of converters is critical for three-phase machine drives [4]. Power converter switch failures can be generally classified as the short circuit and open circuit faults [7]–[9]. Usually, a

Manuscript received December 11, 2018; accepted February 9, 2019. Date of publication February 25, 2019; date of current version August 29, 2019. Recommended for publication by Associate Editor L. Dallesandro. *(Corresponding author: S.Gh Seifossadat.)*

The authors are with the Department of Electrical Engineering, Faculty of Engineering, Shahid Chamran University of Ahvaz, Ahvaz 61357-43337, Iran (e-mail:

–speed regions, the fault harmonic and other nonlinear harmonic effects could be discriminated clearly. Hence, these approaches can easily detect the fault. However, at low speed, the operating frequencies are quite low to effectively separate them from the fault harmonics. Hence, fault detection might fail when adopting FFT to diagnose the fault at low speed operating conditions. On the other hand, the fault harmonic spectrum analysis becomes more difficult in the transient regime [13], [22]. It is noteworthy that the converter switch failures primarily occur due to the high rates of switching spikes (dv/dt) during transients. For such conditions, frequency-domain approaches may not provide perfect fault detection for variable frequency drives. By contrast, the time-domain signal processing approaches are much more efficient for such transients and for load disturbances [22], [23]. A common time-domain open-phase fault-detection technique is to calculate the root-mean square (RMS) values of three-phase stator currents over a fundamental period [14]–[18]. In this technique, a current residual value is considered for fault detection. When the residual value exceeds the predefined threshold, a fault indication signal is generated. In rms-based methods, the detection signal is triggered at least one electrical cycle after the fault inception. Hence, a significantly large memory is required in low-speed regions to activate the fault-detection algorithm. A cost-effective rms-based approach has recently been proposed in [18]. In this method, a zero-voltage vector sampling approach is applied to reconstruct the phase currents and generate diagnostic variables. For an induction or synchronous motor drive which is controlled using FOC, the faulty phase could be found by measuring phase currents and applying the arctangent function of stator current *d–q* components [19]. When the drive is operating near the full-load condition, this method may easily detect the faulty phase. However, diagnostic accuracy is attenuated under no-load and light load operations. To overcome this shortcoming, some approaches were developed based on the neutral point (NP) voltage measurement [20]–[23]. In [20], an open-phase fault detection and discrimination scheme based on zero-sequence voltage component has been proposed for the PMSM drive systems. A similar fault diagnosis method has also been developed in [21] to detect interturn faults. In the presented technique, the zero sequence of both voltage and current components are utilized. In [22], the induced fault harmonic in NP voltage is measured to identify the faulty phase. In addition, a fault-tolerant driving control strategy is employed to enable the drive to continue during the fault. Moreover, the harmonics in both *d–q* currents and the NP voltage are analyzed in [23] to detect the open phase. Although in these methods a higher level of detection performance is achieved, these methods require additional voltage sensors or electrical circuits, resulting in significant system cost and complexity.

Considering all the aforementioned drawbacks, this paper presents a novel time-domain open-circuit fault-diagnostic scheme based on analyzing the *d–q* currents in the second-order rotor-reference frame for vector-controlled drives. The SORP transformation of *d–q* current signals contains information needed to detect and locate the open-phase. Employing the second-order reference frame signals, the open-phase faults could be detected within a half electrical cycle. The fault

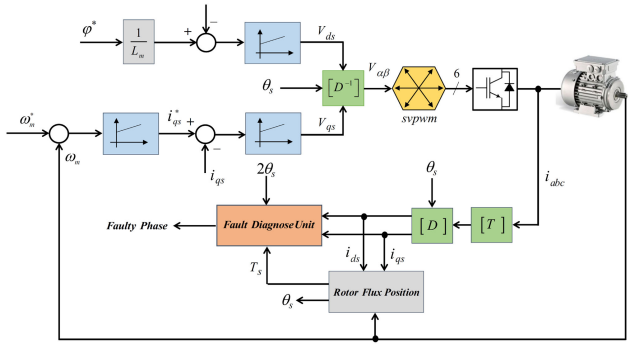

Fig. 1. Schematic diagram of the three-phase induction machine under field-oriented control drive together with the proposed fault diagnosis scheme.

-diagnosis system has been developed regarding its applications in industrial electric drives. The developed system identifies and locates the open-phase faults for condition monitoring and triggers fault-tolerant control schemes. The proposed scheme is effective over the whole speed range and for any loading condition, contrary to the previously proposed methods, e.g., [19]. A significantly less amount of computation or memory storage is required than the rms-based methods [14]–[18], avoiding the use of additional sensors and the increase of drive system cost and complexity [22], [23]. Thus, the proposed method is suitable for low-cost motor drive systems. The performance of the proposed scheme has been analyzed through experimental tests on a sample three-phase induction machine. However, it can be implemented on six-phase machines configured with two isolated neutrals, by extending the Clarke and Park transformations in these machines.

The second part of this paper explains the SORP transformation mathematically. In Section III, the proposed fault diagnostic scheme is described in detail. Verification of the fault detection performance is presented through hardware implementation in Section IV. Finally, the last section provides the main conclusions.

II. Proposed Open-Phase Fault Detection Method

This part describes the mathematical analysis of the three-phase induction machine during an open-phase fault. Practically, it is desirable that the fault detection scheme employs *d–q* currents which already are available from the prime FOC control system. The fault detection unit is independent of the drive system, so it can be easily embedded as a subsystem. Fig. 1 illustrates the field-oriented SVPWM drive system combined with the fault diagnosis unit which detects and locates the open-phase faults.

A. Analysis of d–q Currents in Healthy Operation

When the induction motor is driven by a healthy voltage-source inverter, the three-phase symmetrical current waveforms are as follows:

$$\begin{cases} i_a = I_{m_1}\cos(\omega_s t + \varphi) \\ i_b = I_{m_1}\cos(\omega_s t - 2\pi/3 + \varphi) \\ i_c = I_{m_1}\cos(\omega_s t + 2\pi/3 + \varphi) \end{cases} \quad (1)$$

where ω_s is the phase current frequency, I_{m1} the amplitude of each phase current in healthy condition, and φ the initial phase angle which is also the load angle in healthy condition. In the field-oriented control scheme, the three-phase quantities are transferred to α–β–o currents based on Clarke transformation

$$[T] = \frac{2}{3}\begin{bmatrix} 1 & -1/2 & -1/2 \\ 0 & \sqrt{3}/2 & -\sqrt{3/2} \\ 0.5 & 0.5 & 0.5 \end{bmatrix} \tag{2}$$

$$\begin{bmatrix} i_\alpha & i_\beta & i_o \end{bmatrix}^T = [T].\begin{bmatrix} i_a & i_b & i_c \end{bmatrix}^T. \tag{3}$$

The core part of FOC is the rotor flux position, θ_s which is calculated as [36]

$$\theta_s = \int \omega_s.dt = \int \left(p.\omega_m + \frac{i_q}{T_r\, i_d}\right).dt \tag{4}$$

where ω_m is the rotor speed, p the machine pole pairs, and T_r is the rotor time constant. The rotational park transformation [D], converts the α–β subspace to the d–q plane

$$[D] = \begin{bmatrix} \cos\theta_s & \sin\theta_s \\ -\sin\theta_s & \cos\theta_s \end{bmatrix} \tag{5}$$

$$\begin{bmatrix} i_d & i_q \end{bmatrix}^T = [D].\begin{bmatrix} i_\alpha & i_\beta \end{bmatrix}^T. \tag{6}$$

Using the generalized park transformation, the three-phase motor currents are transformed to two orthogonal components in the field-oriented control. Therefore, in healthy operation, the d–q currents can be expressed as

$$\begin{cases} I_d = I_{m_1}\cos\varphi \\ I_q = I_{m_1}\sin\varphi \end{cases} \tag{7}$$

Theoretically, the load angle φ remains between 0 and 90 degrees for an induction motor under healthy condition. At no-load condition, φ is close to zero; thus, the torque component current, i_q is nearly zero [23]. According to the principle of the FOC scheme, the flux component current, i_d is controlled to keep it, the same as its value at no-load condition ($\varphi = 0$) i.e., $i_d = I_m$. However, when the motor is loaded, both of I_{m1} and φ increase, resulting in an increment in i_q. By contrast, i_d nearly remains constant as I_{m1} increases and $\cos(\varphi)$ decreases under field-oriented condition (See Fig. 2).

B. Analysis of d–q Currents in Faulty Operation

It is possible to accomplish the theoretical analysis of the fault condition by expressing the post-fault equations for the other healthy phases. It is assumed that open phase occurs in phase a, i.e., $i_a = 0$ and $i_b = -i_c = -I_{m_2}\cos(\omega_s t + \varphi_a)$. According to (3) and (6), i_d and i_q should be modified in faulty condition as follows:

$$\begin{cases} I_{d_{a-\text{fault}}} = -\frac{\sqrt{3}}{3} I_{m_2}\sin(2\theta + \varphi_a) + \underbrace{\frac{\sqrt{3}}{3} I_{m_2}\sin(\varphi_a)}_{\text{DC Value}} \\ I_{q_{a-\text{fault}}} = -\frac{\sqrt{3}}{3} I_{m_2}\cos(2\theta + \varphi_a) - \underbrace{\frac{\sqrt{3}}{3} I_{m_2}\cos(\varphi_a)}_{\text{DC Value}}. \end{cases} \tag{8}$$

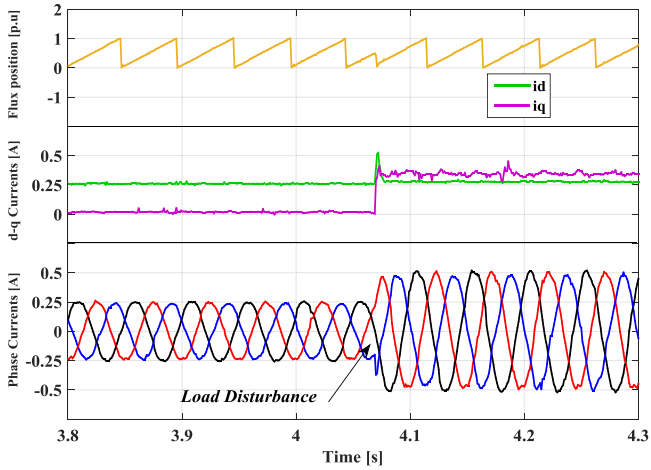

Fig. 2. Induction motor currents at no-load and 45% of load (Experiment test at 500 rpm speed reference).

Similarly, for the faulty phase b; $i_c = -i_a = -I_{m_2}\cos(\omega_s t + \varphi_b)$

$$\begin{cases} I_{d_{b-\text{fault}}} = \frac{\sqrt{3}}{6} I_{m_2}\sin(2\theta + \varphi_b) + \frac{1}{2} I_{m_2}\cos(2\theta + \varphi_b) \\ \qquad - \underbrace{\frac{\sqrt{3}}{6} I_{m_2}\sin(\varphi_b) + \frac{1}{2} I_{m_2}\cos(\varphi_b)}_{\text{DC Value}} \\ I_{q_{b-\text{fault}}} = -\frac{1}{2} I_{m_2}\sin(2\theta + \varphi_b) + \frac{\sqrt{3}}{6} I_{m_2}\cos(2\theta + \varphi_b) \\ \qquad + \underbrace{\frac{1}{2} I_{m_2}\sin(\varphi_b) + \frac{\sqrt{3}}{6} I_{m_2}\cos(\varphi_b)}_{\text{DC Value}} \end{cases}. \tag{9}$$

And for the faulty phase c; $i_a = -i_b = -I_{m_2}\cos(\omega_s t + \varphi_c)$

$$\begin{cases} I_{d_{c-\text{fault}}} = \frac{\sqrt{3}}{6} I_{m_2}\sin(2\theta + \varphi_c) - \frac{1}{2} I_{m_2}\cos(2\theta + \varphi_c) \\ \qquad - \underbrace{\frac{\sqrt{3}}{6} I_{m_2}\sin(\varphi_c) - \frac{1}{2} I_{m_2}\cos(\varphi_c)}_{\text{DC Value}} \\ I_{q_{c-\text{fault}}} = \frac{1}{2} I_{m_2}\sin(2\theta + \varphi_c) + \frac{\sqrt{3}}{6} I_{m_2}\cos(2\theta + \varphi_c) \\ \qquad - \underbrace{\frac{1}{2} I_{m_2}\sin(\varphi_c) + \frac{\sqrt{3}}{6} I_{m_2}\cos(\varphi_c)}_{\text{DC Value}} \end{cases} \tag{10}$$

where φ_a, φ_b, and φ_c are, respectively, the post-fault phase angles related to faulty phase a, b, and c conditions. In (8), (9) and (10), I_{m_2} is the current amplitude in the fault condition. Analytically, it can be seen from the above fault equations that due to the open-phase fault, an oscillating signal with a frequency equal to twice of the fundamental frequency appears in both i_d and i_q [23]. However, the positive pre-fault dc (average value) related to the load condition is not affected by the fault [19] (See Fig. 3).

Taking the effect of current phase angle variations under healthy condition($0 \le \varphi \le \pi/2$)and comparing dc values of pre/post-fault equations, the phase angle variations under

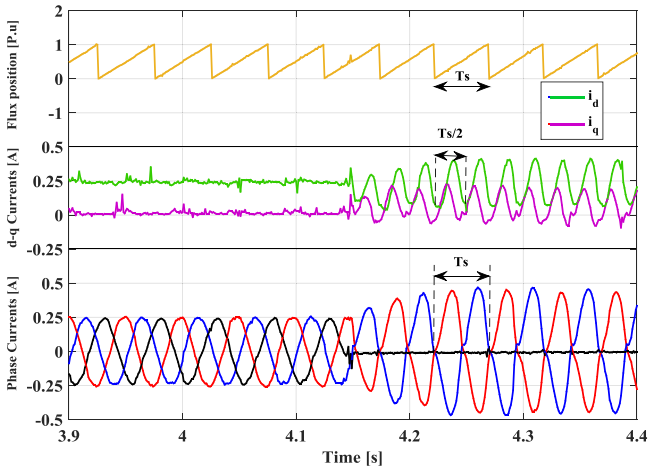

Fig. 3. Induction motor currents in pre- and post-fault conditions (Experiment test at 500 rpm speed reference and no load).

post-fault condition should be as follows:

$$\begin{cases} \pi/2 \le \varphi_a \le \pi \\ -\pi/6 \le \varphi_b \le \pi/3 \\ -5\pi/6 \le \varphi_c \le -\pi/3. \end{cases} \tag{11}$$

As seen in (11), different phase angles are observed for the two remained healthy phases under the fault condition. Phase angles are shifted by 90, -30, and -150 degrees for fault in phase *a*, *b*, and *c*, respectively.

III. Derivation of the Fault Diagnosis Scheme

A. The d–q Currents in Second-Order Reference Frame

According to the above equations, *d–q* currents under the faulty condition and α–β currents under the healthy condition proceed in the same manner, i.e., there is 90° phase shift between them. The rotational second-order park transformation [$D_{2\theta}$], converts the $(d–q)_\theta$ subspace to the $(d–q)_{2\theta}$ plane. These two new variables presented here, provide efficient fault detection and localization in a three-phase machine

$$[D_{2\theta}] = \begin{bmatrix} \cos 2\theta_s & \sin 2\theta_s \\ -\sin 2\theta_s & \cos 2\theta_s \end{bmatrix} \tag{12}$$

$$\begin{bmatrix} i_{d_{(2_\theta)}} \\ i_{q_{(2_\theta)}} \end{bmatrix} = \begin{bmatrix} \cos 2\theta_s & \sin 2\theta_s \\ -\sin 2\theta_s & \cos 2\theta_s \end{bmatrix} \begin{bmatrix} i_{d_{(\theta)}} \\ i_{q_{(\theta)}} \end{bmatrix}. \tag{13}$$

Applying the proposed second-order rotational park transformation to the (7), (8), (9), and (10), i_d and i_q in the second-order rotor reference frame are calculated as follows:

1) Healthy Operation:

$$\begin{cases} I_{d_{(2_\theta)}} = I_{m_1} \cos(2\theta - \varphi) \\ I_{q_{(2_\theta)}} = -I_{m_1} \sin(2\theta - \varphi). \end{cases} \tag{14}$$

As seen in (14), pure sinusoidal waveforms are produced by applying the SORP transformation, in $(d–q)_{2\theta}$ currents. Hence, the average value of the $I_{d(2\theta)}$ and $I_{q(2\theta)}$ under normal operation take zero values within half period of the fundamental period

$$\overline{I}_{dq_{(2_\theta)}} = \frac{2}{T_s} \int_t^{t+T_s/2} I_{dq_{(2_\theta)}}.dt \simeq 0 \tag{15}$$

where $\bar{I}_{dq(2\theta)}$ is the average value of $(d–q)_{2\theta}$ currents within a half cycle. Therefore, the average absolute values higher than a predefined threshold could be considered for registering a fault.

2) Faulty operation: The detection variables $\bar{I}_{dq(2\theta)}$ just identify the open phase fault. In order to locate the faulty phase, the $I_{d(2\theta)}$ and $I_{q(2\theta)}$ could be investigated in open-phase fault occurrence.

For $i_a = 0$

$$\begin{cases} I_{d_{(2_\theta)}} = \tilde{I}_{d_{(2_\theta)}} + \bar{I}_{d_{(2_\theta)}} = -\frac{\sqrt{3}}{3} I_{m_2} \cos(2\theta + \varphi_a) \\ \qquad - \underbrace{\frac{\sqrt{3}}{3} I_{m_2} \cos(\varphi_a)}_{\bar{I}_{d_{(2_\theta)}}} \\ I_{q_{(2_\theta)}} = \tilde{I}_{q_{(2_\theta)}} + \bar{I}_{q_{(2_\theta)}} = \frac{\sqrt{3}}{3} I_{m_2} \sin(2\theta - \varphi_a) \\ \qquad - \underbrace{\frac{\sqrt{3}}{3} I_{m_2} \sin(\varphi_a)}_{\bar{I}_{q_{(2_\theta)}}}. \end{cases} \tag{16}$$

And for $i_b = 0$

$$\begin{cases} I_{d_{(2_\theta)}} = \tilde{I}_{d_{(2_\theta)}} + \bar{I}_{d_{(2\theta)}} = \frac{1}{2} I_{m_2} \sin(2\theta + \varphi_b) + \frac{\sqrt{3}}{6} I_{m_2} \\ \qquad \times \cos(2\theta + \varphi_b) - \underbrace{\frac{1}{2} I_{m_2} \sin(\varphi_b) + \frac{\sqrt{3}}{6} I_{m_2} \cos(\varphi_b)}_{\bar{I}_{d_{(2_\theta)}}} \\ I_{q_{(2_\theta)}} = \tilde{I}_{q_{(2_\theta)}} + \bar{I}_{q_{(2_\theta)}} = -\frac{\sqrt{3}}{6} I_{m_2} \sin(2\theta + \varphi_b) + \frac{1}{2} I_{m_2} \\ \qquad \times \cos(2\theta + \varphi_b) + \underbrace{\frac{\sqrt{3}}{6} I_{m_2} \sin(\varphi_b) + \frac{1}{2} I_{m_2} \cos(\varphi_b)}_{\bar{I}_{q_{(2_\theta)}}}. \end{cases} \tag{17}$$

And for $i_c = 0$

$$\begin{cases} I_{d_{(2_\theta)}} = \tilde{I}_{d_{(2_\theta)}} + \bar{I}_{d_{(2_\theta)}} = -\frac{1}{2} I_{m_2} \sin(2\theta + \varphi_c) + \frac{\sqrt{3}}{6} I_{m_2} \\ \qquad \times \cos(2\theta + \varphi_c) + \underbrace{\frac{1}{2} I_{m_2} \sin(\varphi_c) - \frac{\sqrt{3}}{6} I_{m_2} \cos(\varphi_c)}_{\bar{I}_{d_{(2_\theta)}}} \\ I_{q_{(2_\theta)}} = \tilde{I}_{q_{(2_\theta)}} + \bar{I}_{q_{(2_\theta)}} = -\frac{\sqrt{3}}{6} I_{m_2} \sin(2\theta + \varphi_c) - \frac{1}{2} I_{m_2} \\ \qquad \times \cos(2\theta + \varphi_c) + \underbrace{\frac{\sqrt{3}}{6} I_{m_2} \sin(\varphi_c) - \frac{1}{2} I_{m_2} \cos(\varphi_c)}_{\bar{I}_{q_{(2_\theta)}}} \end{cases} \tag{18}$$

where $\tilde{I}_{dq(2\theta)}$ and $\bar{I}_{dq(2\theta)}$ are the $(d–q)_{2\theta}$ oscillating and average terms in fault condition, respectively.

To mitigate associated problems with the transients, and to set the same thresholds for various speed drives with

TABLE I
PER UNIT NORMALIZED *d–q* AVERAGE VALUES VERSUS PHASE ANGLE VARIATIONS IN NORMAL REFERENCE FRAME

Healthy			Phase a-Fault			Phase b-Fault			Phase c-Fault		
φ	$\overline{I}_d^{pu}$	$\overline{I}_q^{pu}$	φ_a	$\overline{I}_d^{pu}$	$\overline{I}_q^{pu}$	φ_b	$\overline{I}_d^{pu}$	$\overline{I}_q^{pu}$	φ_c	$\overline{I}_d^{pu}$	$\overline{I}_q^{pu}$
0	1	0	**1.57**	1	0	**-0.52**	1	0	**-2.61**	1	0
0.1	0.995	0.0998	**1.7**	0.9917	0.1288	**-0.3**	0.9751	0.2217	**-2.4**	0.9763	0.2163
0.3	0.9553	0.2955	**1.9**	0.9463	0.3233	**-0.1**	0.911	0.411	**-2.2**	0.9139	0.4059
0.5	0.8776	0.4794	**2.1**	0.8632	0.5048	**0.1**	0.8118	0.584	**-2**	0.815	0.5794
0.7	0.7648	0.6442	**2.3**	0.7457	0.6663	**0.3**	0.6796	0.7336	**-1.8**	0.6837	0.7298
0.9	0.6216	0.7833	**2.5**	0.5985	0.8011	**0.5**	0.5203	0.854	**-1.6**	0.5251	0.8511
1.1	0.4536	0.8912	**2.7**	0.4274	0.9041	**0.7**	0.3403	0.9403	**-1.4**	0.3455	0.9384
1.3	0.2675	0.9636	**2.9**	0.2392	0.971	**0.9**	0.1467	0.9892	**-1.2**	0.1522	0.9883
1.57	0	1	**3.14**	0	1	**1.04**	0	1	**-1.047**	0	1

TABLE II
PER UNIT NORMALIZED *d–q* AVERAGE VALUES VERSUS PHASE ANGLE VARIATIONS IN SECOND-ORDER REFERENCE FRAME

Healthy			Phase a-Fault			Phase b-Fault			Phase c-Fault		
φ	$\overline{I}_{d(2\theta)}^{pu}$	$\overline{I}_{q(2\theta)}^{pu}$	φ_a	$\overline{I}_{d(2\theta)}^{pu}$	$\overline{I}_{q(2\theta)}^{pu}$	φ_b	$\overline{I}_{d(2\theta)}^{pu}$	$\overline{I}_{q(2\theta)}^{pu}$	φ_c	$\overline{I}_{d(2\theta)}^{pu}$	$\overline{I}_{q(2\theta)}^{pu}$
0	0	0	**1.57**	0	-1	**-0.52**	0.866	0.5	**-2.61**	-0.866	0.5
0.1	0	0	**1.7**	0.1289	-0.9915	**-0.3**	0.7335	0.6796	**-2.4**	-0.9536	0.3008
0.3	0	0	**1.9**	0.3233	-0.9461	**-0.1**	0.5838	0.8117	**-2.2**	-0.9943	0.1055
0.5	0	0	**2.1**	0.5048	-0.8632	**0.1**	0.411	0.9068	**-2**	-0.9955	-0.0942
0.7	0	0	**2.3**	0.6663	-0.7456	**0.3**	0.2217	0.9751	**-1.8**	-0.9569	-0.2901
0.9	0	0	**2.5**	0.801	-0.5984	**0.5**	0.0236	0.9997	**-1.6**	-0.8802	-0.4745
1.1	0	0	**2.7**	0.9041	-0.4273	**0.7**	-0.1754	0.9844	**-1.4**	-0.7648	-0.6399
1.3	0	0	**2.9**	0.9709	-0.2392	**0.9**	-0.3675	0.9299	**-1.2**	-0.6259	-0.7797
1.57	0	0	**3.14**	1	0	**1.04**	-0.5	0.866	**-1.047**	-0.5	-0.866

variable current amplitudes, the normalization is conducted. The per unit normalization is carried out by dividing each average value of $I_{d(2\theta)}$ and $I_{q(2\theta)}$ by current Park vector in the second-order reference frame, and peak values of the currents in (14)

$$\left|\overline{I}_{s_{(2\theta)}}\right| = \frac{\sqrt{3}}{3}\sqrt{i_{d_{(2\theta)}}^2 + i_{q_{(2\theta)}}^2}. \tag{19}$$

The per unit normalized *d–q* currents in the second-order reference frame can be formulated as

$$I_{d-q_{(2\theta)}}^{pu} = \frac{I_{(d-q)_{2\theta}}}{\left|\overline{I}_{s_{(2\theta)}}\right|} \tag{20}$$

where $I_{d-q(2\theta)}^{pu}$ is the normalized per unit *d–q* current in the second-order reference frame. As a result of normalization, the dc values fall into [0, 1], and the variables become independent of currents amplitude. Finally, the normalized per unit $I_{d(2\theta)}$ and $I_{q(2\theta)}$ currents under faulty condition could be rewritten as;

For $i_a = 0$

$$\begin{cases} I_{d_{(2\theta)}}^{pu} = \tilde{I}_{d_{(2\theta)}}^{pu} + \bar{I}_{d_{(2\theta)}}^{pu} = -\cos(2\theta + \varphi_a) - \underbrace{\cos(\varphi_a)}_{\bar{I}_{d_{(2\theta)}}^{pu}} \\ I_{q_{(2\theta)}}^{pu} = \tilde{I}_{q_{(2\theta)}}^{pu} + \bar{I}_{q_{(2\theta)}}^{pu} = \sin(2\theta - \varphi_a) - \underbrace{\sin(\varphi_a)}_{\bar{I}_{q_{(2\theta)}}^{pu}}. \end{cases} \tag{21}$$

And for $i_b = 0$

$$\begin{cases} I_{d_{(2\theta)}}^{pu} = \tilde{I}_{d_{(2\theta)}}^{pu} + \bar{I}_{d_{(2\theta)}}^{pu} = \frac{\sqrt{3}}{2}\sin(2\theta + \varphi_b) \\ \quad + \frac{1}{2}\cos(2\theta + \varphi_b) - \underbrace{\frac{\sqrt{3}}{2}\sin(\varphi_b) + \frac{1}{2}\cos(\varphi_b)}_{\bar{I}_{d_{(2\theta)}}^{pu}} \\ I_{q_{(2\theta)}}^{pu} = \tilde{I}_{q_{(2\theta)}}^{pu} + \bar{I}_{q_{(2\theta)}}^{pu} = -\frac{1}{2}\sin(2\theta + \varphi_b) \\ \quad + \frac{\sqrt{3}}{2}\cos(2\theta + \varphi_b) + \underbrace{\frac{1}{2}\sin(\varphi_b) + \frac{\sqrt{3}}{2}\cos(\varphi_b)}_{\bar{I}_{q_{(2\theta)}}^{pu}}. \end{cases} \tag{22}$$

And for $i_c = 0$

$$\begin{cases} I_{d_{(2\theta)}}^{pu} = \tilde{I}_{d_{(2\theta)}}^{pu} + \bar{I}_{d_{(2\theta)}}^{pu} = -\frac{\sqrt{3}}{2}\sin(2\theta + \varphi_c) \\ \quad + \frac{1}{2}\cos(2\theta + \varphi_c) + \underbrace{\frac{\sqrt{3}}{2}\sin(\varphi_c) + \frac{1}{2}\cos(\varphi_c)}_{\bar{I}_{d_{(2\theta)}}^{pu}} \\ I_{q_{(2\theta)}}^{pu} = \tilde{I}_{q_{(2\theta)}}^{pu} + \bar{I}_{q_{(2\theta)}}^{pu} = -\frac{1}{2}\sin(2\theta + \varphi_c) \\ \quad - \frac{\sqrt{3}}{2}\cos(2\theta + \varphi_c) + \underbrace{\frac{1}{2}\sin(\varphi_c) - \frac{\sqrt{3}}{2}\cos(\varphi_c)}_{\bar{I}_{q_{(2\theta)}}^{pu}}. \end{cases} \tag{23}$$

As mentioned, the dc values of the *d–q* currents are not affected by any open-phase fault condition (*a*, *b,* or *c*) and vary only upon the load condition. However, the fault localization

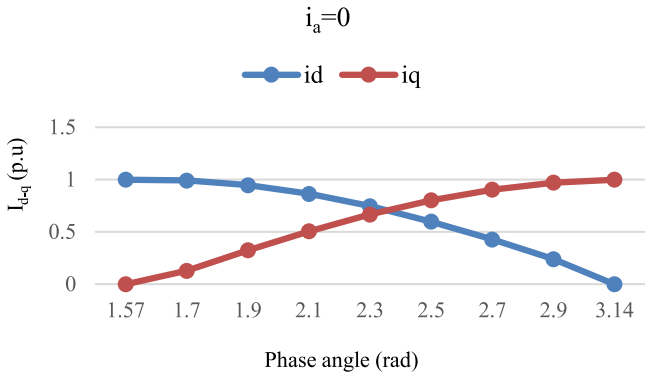

Fig. 4. $\bar{I}_{dq}$ variations in fault condition based on normal park transformation against the phase angle for each fault scenario.

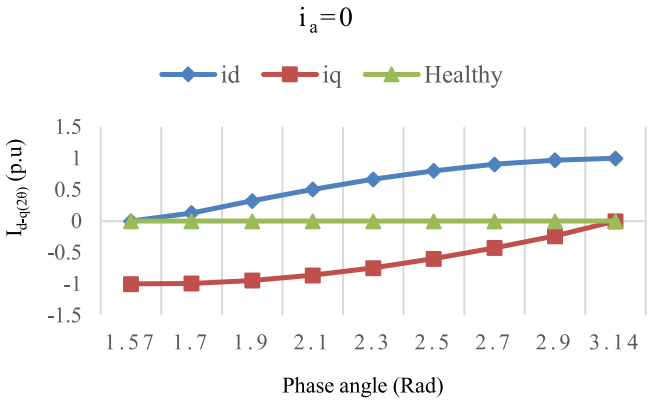

Fig. 5. $\overline{I}^{pu}_{dq(2\theta)}$ variations against the post-fault phase angle (φ_a) concerning the phase-*a* open-phase fault.

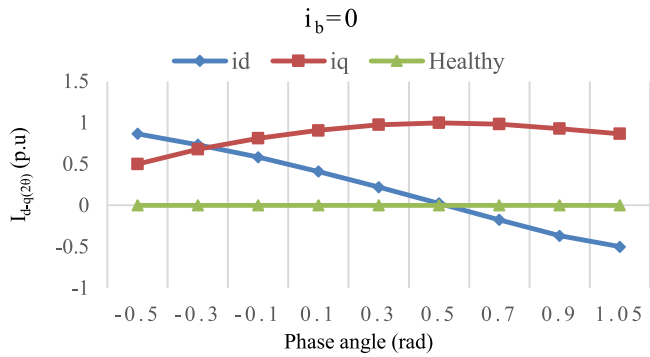

Fig. 6. $\overline{I}^{pu}_{dq(2\theta)}$ variations against the post-fault phase angle (φ_b) concerning the phase-*b* open-phase fault.

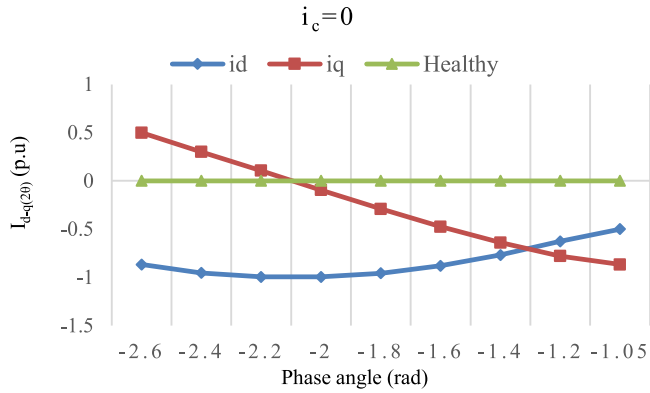

Fig. 7. $\overline{I}^{pu}_{dq(2\theta)}$ variations against the post-fault phase angle (φ_c) concerning the phase-*c* open-phase fault.

method for each fault scenario has a distinct symptom for $(d$–$q)_{2\theta}$ currents. The summary of $\overline{I}^{pu}_{d}$, $\overline{I}^{pu}_{q}$, $\overline{I}^{pu}_{d(2\theta)}$, and $\overline{I}^{pu}_{q(2\theta)}$ values under healthy and faulty conditions concerning the phase angle variations have been provided in Tables I and II. As can be observed, the same results could be observed in $\overline{I}^{pu}_{d}$, $\overline{I}^{pu}_{q}$ for each fault scenario while $\overline{I}^{pu}_{d(2\theta)}$ and $\overline{I}^{pu}_{d(2\theta)}$ take different values for each fault condition. As an example, the behavior of the dc values of d–q currents against the phase angle in the normal reference frame is represented in Fig. 4 for the open-phase fault in phase $a(\pi/2 \le \varphi_a \le \pi)$. By contrast, the $\overline{I}^{pu}_{d(2\theta)}$ and $\overline{I}^{pu}_{q(2\theta)}$ values for three open phase fault scenarios do not have the same variation pattern (see Figs. 5–7). This is the theoretical basis of fault localization for the proposed fault-detection scheme.

B. Fault Localization Strategy

Regarding the open-phase faults, specific characteristics corresponding to the faulty phase will provide the open-phase fault diagnosis and localization. All the detection variables are close to zero during the normal operating conditions. However, when the fault occurs, the $\overline{I}^{\mathrm{pu}}_{d(2\theta)}$ and $\overline{I}^{\mathrm{pu}}_{q(2\theta)}$ values carry diagnostic information about the faulty phase. Unlike the normal reference frame, they allow performing a different evolution of the fault indexes. Based on the difference between these average values, the faulty phase can be effectively detected. As seen in Fig. 5, the $\overline{I}^{\mathrm{pu}}_{q(2\theta)}$ stays at values close to zero under healthy condition. However, it gets "-1" value at the no-load condition as $\overline{I}^{\mathrm{pu}}_{d(2\theta)}$ take unity value for highest load magnitudes when phase a is opened. The unique pattern is obtained for fault in phase b that $\overline{I}^{\mathrm{pu}}_{q(2\theta)}$ take values above 0.5 under different load conditions (see Fig. 6). On the other hand, for fault detection in phase c, the value of $\overline{I}^{\mathrm{pu}}_{d(2\theta)}$ can be considered as a fault indicator that will take negative values below -0.5 for all range of operating conditions (see Fig. 7). It is noteworthy that the fault signatures also allow determining the severity of fault according to the load angle behavior. Finally, the fault symptom variables that allow performing the fault diagnosis are listed in Table III.

TABLE III
DIAGNOSTIC SIGNALS UNDER DIFFERENT OPEN-PHASE FAULT CONDITIONS

Fault Condition	Fault Signatures
Phase-a Fault	$(-1-\gamma \le \overline{I}^{pu}_{q_{(2\theta)}} < 0+\gamma), \& (0-\gamma \le \overline{I}^{pu}_{d_{(2\theta)}} \le 1+\gamma)$
Phase-b Fault	$(0.5-\gamma \le \overline{I}^{pu}_{q_{(2\theta)}} \le 1+\gamma) \& (-0.5-\gamma \le \overline{I}^{pu}_{d_{(2\theta)}} \le \sqrt{3}/2+\gamma)$
Phase-c Fault	$(-\sqrt{3}/2-\gamma \le \overline{I}^{pu}_{q_{(2\theta)}} \le 0.5+\gamma) \& (-1-\gamma \le \overline{I}^{pu}_{d_{(2\theta)}} \le -0.5+\gamma)$
Healthy	$\lvert \overline{I}^{pu}_{dq_{(2\theta)}} \rvert \le \sigma$

To obtain more accuracy in fault detection and generate a distinct fault index, the security margin is also set to compensate

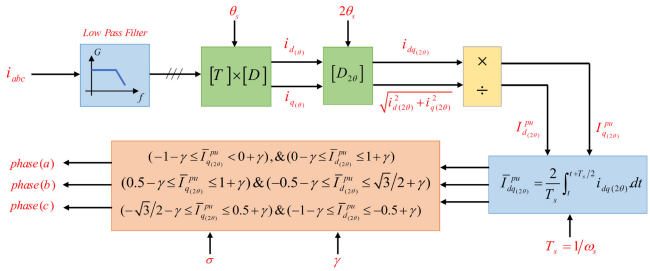

Fig 8. Schematic representation of the proposed fault diagnosis method.

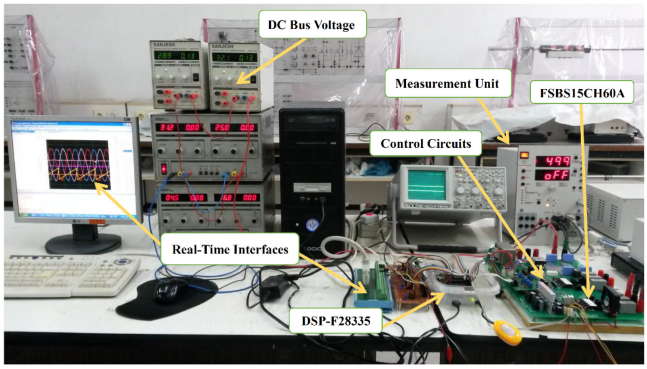

Fig. 9. Experimental test rig.

for the undesirable features in electric drives and computation errors [35], [37].

The threshold margins γ and σ have been taken for high immunity to false alarms in both healthy and faulty operations. These values were experimentally established for fault detection in the whole operating range under different load conditions. It is also possible to decrease the value of σ if the accuracy of T_s is ensured in the drive regulated with FOC. This detection procedure involves the following steps:

1) Computing the $(d–q)_{2\theta}$ currents using the SORP transformation;
2) Normalization of $(d–q)_{2\theta}$ currents based on current park vector;
3) Integration of the $(d–q)_{2\theta}$ current signals over the half electrical period;
4) Analyzing the average values to detect and locate the faulty phase.

The described fault diagnostic scheme is summarized in Fig. 8. The experimental investigation of the proposed method is reported in the next section to verify the trends of theoretical analysis.

IV. Experimental Results

To verify the capabilities of the proposed method, an experimental platform is established. Figs. 9 and 10 describe the real-time data acquisition system and the test bench platform used for experiments. Due to the limitations of power used in the laboratory, the VSCs are connected to a 180 V dc bus voltage. The SVPWM VSI is provided by a high-performance integrated IGBT inverter module Fairchild FSBS15CH60. The three-phase induction machine is coupled with a dc machine

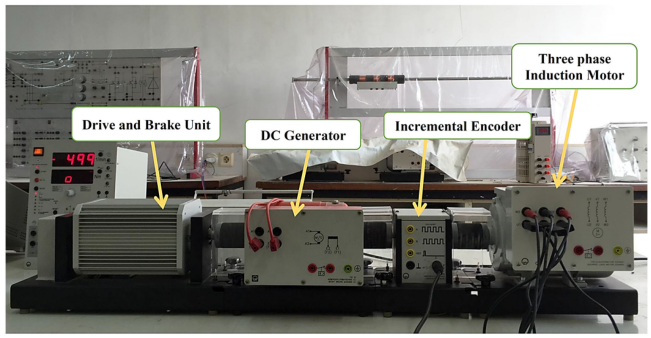

Fig. 10. Three-phase induction motor coupled to the dc machine and recording equipments.

TABLE IV
Three-Phase Induction Machine Specifications

Machine Parameters	Value
Rated power	250 W
Rated voltage(V_n)	230 V
Rated current (I_n)	0.76 A
Rated speed (N_m)	1350 rpm
Stator Resistant(R_s)	42. 00 Ω
Rotor Resistant (R_r)	23. Ω
Stator Inductance (L_s)	10.16 mH
Rotor Inductance (L_r)	10.16 mH
Mutual Inductance (M)	18.50 mH
Number of pole pairs(P)	2

as a step load and the equipment sets used for recording and monitoring the electrical characteristics of the machines. The SVPWM frequency, as well as current sampling frequency, is 10-kHz.

The field-oriented control and fault detection techniques were implemented by a 32-bit DSP; TMS320F28335 from Texas Instruments. Experimental data were captured using an Advantech Real-Time data acquisition device. The modeled system was programmed using Texas Instruments' Code Composer Studio software. Then, the C code is generated and Embedded to DSP for real-time laboratory experiments and processed using MATLAB/Simulink environment. Speed information is derived from a high-resolution encoder with 1024 pulses per turn. Three Honeywell CSNE151-100 hall-effect sensors are employed to obtain the motor currents. To investigate the proposed fault diagnosis performance, the steady-state and dynamic behavior of the drive system under different modes of operation is, presented. The open-phase fault detection performance under speed acceleration, load torque disturbance, and the sensor offset situations are examined. The motor parameters are detailed in Table IV. The open-phase fault condition is performed by manually opening the motor terminal connections.

A. Fault Detection Performance at Light Load Operation

First, the evaluation of the proposed method has been performed under light load operation, at low- and high-speed regions (400 and 1300 rpm) has been performed. The first step in

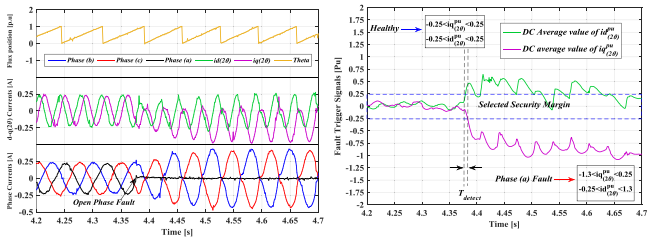

Fig. 11. Fault detection performance when the open-phase fault occurs on phase *a* (400 r/min speed reference and no load).

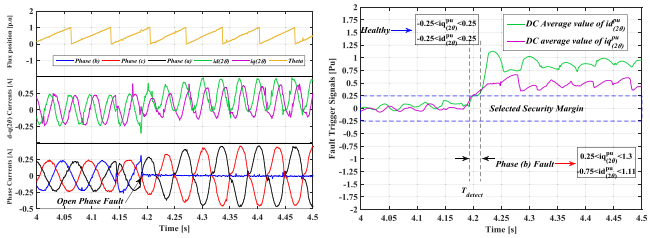

Fig. 12. Fault detection performance when the open-phase fault occurs on phase *b* (400 r/min speed reference and no load).

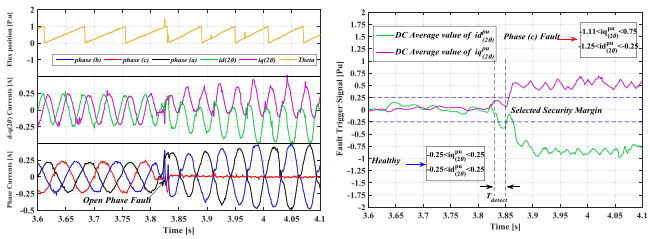

Fig. 13. Fault detection performance when the open-phase fault occurs on phase *c* (400 r/min speed reference and no load).

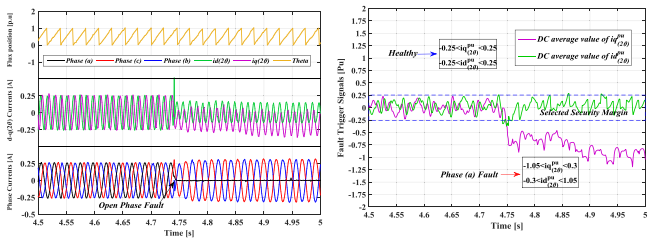

Fig. 14. Fault detection performance when the open-phase fault occurs on phase *a* (1300 r/min speed reference and no load).

experimental tests is to set γ, and σ parameters to define the security margin and threshold values for trustable fault detection. The values of γ and σ in Table III are designed experimentally and set to 0.3, and 0.25, respectively.

To describe time-domain motor phase currents, rotor flux position, and the per unit normalized average values $\overline{I}^{\mathrm{pu}}_{dq(2\theta)}$, the detection indices are shown during the presence of phases "*a*," "*b*," and "c" faults sequentially. It is concluded that fault indexes $\overline{I}^{\mathrm{pu}}_{d(2\theta)}$ and $\overline{I}^{\mathrm{pu}}_{q(2\theta)}$ rapidly converges to certain values whereas in healthy condition remain close to zero value with a small ripple. As seen in Figs. 11–13, $\overline{I}^{\mathrm{pu}}_{q(2\theta)}$ converges to approximately -1, 0.5, and 0.5 and $\overline{I}^{\mathrm{pu}}_{d(2\theta)}$ takes around 0.25, 0.9, and -0.75 values under different fault conditions.

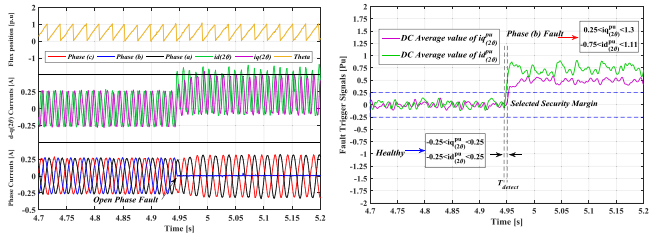

Fig. 15. Fault detection performance when the open-phase fault occurs on phase *b* (1300 r/min speed reference and no load).

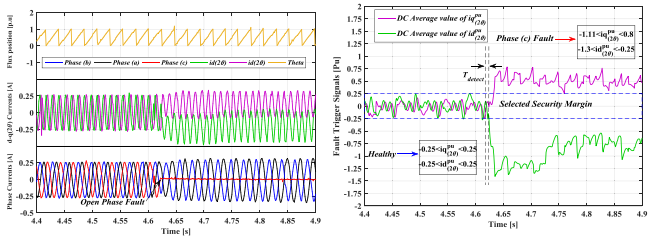

Fig. 16. Fault detection performance when the open-phase fault occurs on phase *c* (1300 r/min speed reference and no load).

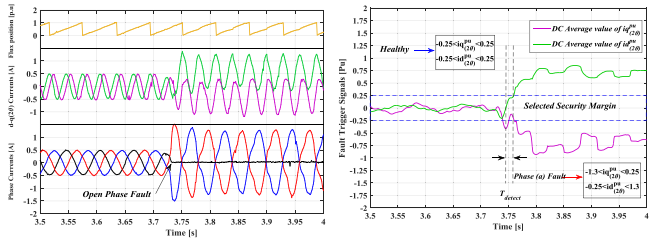

Fig. 17. Fault detection performance when the open-phase fault occurs on phase *a* (500 r/min speed reference and 45% of the load).

These estimated values verify the analysis demonstrated in Section III. It is noticed that observed small oscillations are due to the estimation error in $\omega_{s,}$ and implementation issues. Experimental results show that fault detection time depends upon the speed of operation at the fault occurrence time.

As can be seen from Figs. 11–13, the detection time is in the range of 11 to 16 ms, at the operating speed of 400 rpm. This is corresponding to 13% up to 24% of the motor current fundamental period, respectively. On the other hand, when the open phase fault happens with a mechanical speed of 1300 rpm the fault detection time varies from 6 to 8 ms which is around 26% to 34% of the electrical cycle (See Figs. 14–16).

One of the main difficulties for time-domain fault diagnosis approaches is the fault detection at light load operating conditions. The open-phase fault can be detected in the proposed method even at no load, without using any additional hardware in contrast to the approaches proposed in [19]–[23].

B. Fault Detection Performance at Loaded Operation

The performance of the proposed fault detection approach is evaluated under loaded operation in this part. In this experiment, the motor is controlled to trace the speed of 500-rpm. Regarding the VSI-fed induction motor drive, a load level equivalent to 45% of the motor rated torque, is considered. Figs. 17–19 show the

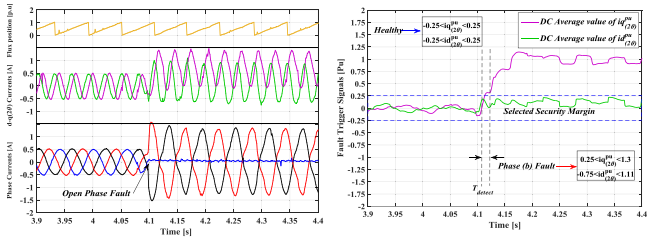

Fig. 18. Fault detection performance when the open-phase fault occurs on phase *b* (500 r/min speed reference and 45% of the load).

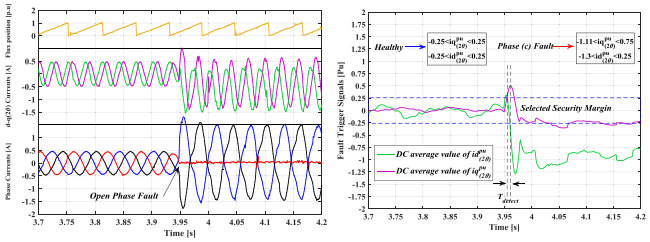

Fig. 19. Fault detection performance when the open-phase fault occurs on phase *c* (500 r/min speed reference and 45% of the load).

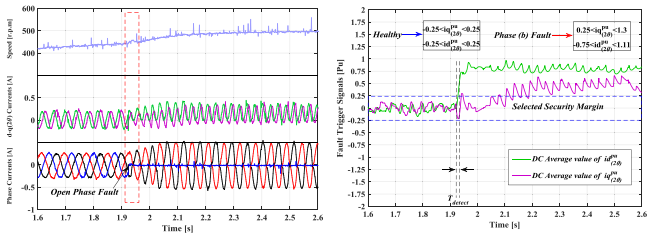

Fig. 20. Fault detection performance during the speed transient regime under phase *b* open-phase fault (500 r/min speed reference).

diagnostic process for the considered operating condition. The open-phase fault is introduced to phase *a*, at $t = 3.747$ s as shown in Fig. 17. As a result, the diagnostic variables $\overline{I}^{\mathrm{pu}}_{d(2\theta)}$ and $\overline{I}^{\mathrm{pu}}_{q(2\theta)}$ converge to 0.75 and -0.65 values that correspond to the fault symptoms described in Table III for fault in phase *a*. When the fault happens on phase *b*, at $t = 4.102$ s, the diagnostic variables $\overline{I}^{\mathrm{pu}}_{d(2\theta)}$ and $\overline{I}^{\mathrm{pu}}_{q(2\theta)}$ converge to 0.1 and 1 values (see Fig. 18). Finally, at $t = 3.95$ s, an open-circuit fault occurs on phase *c*. Clearly, fault indexes $\overline{I}^{pu}_{d(2\theta)}$ and $\overline{I}^{pu}_{q(2\theta)}$ converge to -0.75 and -0.25 values immediately (see Fig. 19). The obtained results perfectly match those obtained in Section III-B. Hence, it is verified that open-phase fault, could be effectively detected and localized under different load conditions.

C. Investigating False Alarms During Speed Transient

In this part, the sensitivity of the fault diagnosis method during the speed transient is examined. Fig. 20 shows time-domain current waveforms and detection variables' behavior. Phase *b* is manually disconnected at $t = 1.92$ s during the acceleration time (start-up time). Consequently, the analogous behavior is observed for fault indices. As seen in Fig. 20, the $\overline{I}^{\mathrm{pu}}_{d(2\theta)}$ and $\overline{I}^{\mathrm{pu}}_{q(2\theta)}$ converge to 0.75 and 0.5, respectively, once the open phase fault is introduced under speed transient. Comparing the fault trigger signals, the $\overline{I}^{\mathrm{pu}}_{d(2\theta)}$ response is observed slower than

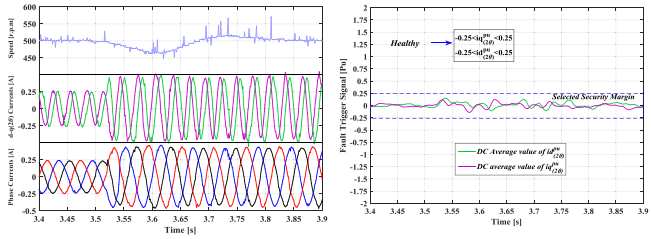

Fig. 21. Open-phase fault detection immunity to load disturbance (500 r/min speed reference).

$\overline{I}^{\mathrm{pu}}_{q(2\theta)}$. However, the proposed scheme detects the fault occurrence almost 10 ms, which is 11% of the motor phase currents' fundamental period. Consequently, the proposed fault detection scheme presents robust behavior under transient modes. Generally, the capability of this method will be guaranteed if the synchronous speed accurately estimated in each sampling period.

D. Investigating False Alarms During Load Disturbance

Fig. 21 shows the corresponding operation of three-phase induction machine under load-torque disturbance. For investigating the accuracy and rapidity of the proposed method under load disturbance, the load torque steps up from no load to about 45% rated load at $t = 3.52$. The speed reference is set to 500 rpm. As can be observed from the experimental test, the fault detection scheme is not affected by the load variation obviously. This shows the robustness against load disturbance. It is noteworthy that the observed small oscillations related to the estimation error in ω_s may not attenuate the capability of the fault detection strategy thanks to the use of security margin.

E. Fault Detection with Phase Current Measurement Error

One of the prevalent issues that may affect the practical applications is the sensor measurement error. As reported in [38], the sensor offset measurement errors might cause the harmonics at twice the fundamental component of stator frequency in a vector controlled motor drive. Therefore, using distorted current/voltage signals may disrupt the fault detection process. To investigate the robustness of the proposed method to current measurement error the following offset components might be considered

$$i_{a-\mathrm{offset}} = a_0,\ i_{b-\mathrm{offset}} = 0,\ i_{c-\mathrm{offset}} = -c_0. \tag{24}$$

In (24), a positive offset on phase *a* sensor and a negative offset is assumed on phase *c* where i_{offset} is the offset error. The *d*–*q* offset currents' components, $i_{d-\mathrm{offset}}$, and $i_{q-\mathrm{offset}}$, can be calculated according to (3) and (6)

$$i_{d-\mathrm{offset}} = \frac{2}{3}a_0\cos(\theta) - \frac{2}{3}c_0\cos\left(\theta + \frac{2\pi}{3}\right) \tag{25}$$

$$i_{q-\mathrm{offset}} = -\frac{2}{3}a_0\sin(\theta) + \frac{2}{3}c_0\sin\left(\theta + \frac{2\pi}{3}\right). \tag{26}$$

By adding (25) and (26) to *d*- and *q*-axis currents, and applying SORP transformation, the following expressions will be

TABLE V
COMPARISON BETWEEN DIFFERENT FAULT DETECTION TECHNIQUES AND THE PROPOSED METHOD

Fault Diagnosis Method	Detection Time	Robustness	Cost	Sensitive to Parameters	Implementation Effort	Computation amount
RMS based methods [14-18]	> 1 cycle	Medium	Low	Low	Low	Medium
Fuzzy based methods [32-34]	≈ 2 cycles	Low	Low	Low	High	High
Model based methods [24-28]	< 1/4 cycle	Low	Low	High	Low	Low
Frequency based method [10-13]	> 1 cycle	Low	Low	Low	Low	Low
Time domain methods [19]	< 1/2 cycle	Low	Low	Low	Low	Low
Time domain+ NP methods [20-23]	≈ 1/4 cycle	High	High	Low	High	High
Proposed method	< 1/2 cycle	High	Low	Low	Low	Low

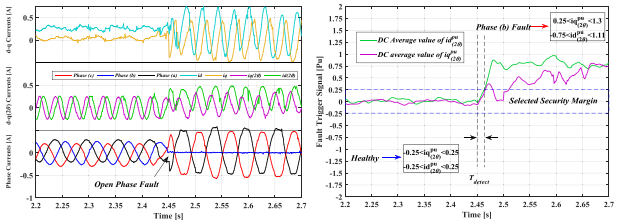

Fig. 22. Open-phase fault detection immunity to current measurement errors (500 r/min speed reference)

added to (14), (16), (17), and (18)

$$i_{d_{(2\theta)-offset}} = \frac{2}{3}a_0\cos(3\theta) - \frac{2}{3}c_0\cos\left(3\theta + \frac{2\pi}{3}\right) \quad (27)$$

$$i_{q_{(2\theta)-\text{offset}}} = -\frac{2}{3}a_0\sin(3\theta) + \frac{2}{3}c_0\sin\left(3\theta + \frac{2\pi}{3}\right). \quad (28)$$

Therefore, the third-order harmonic occurs on $(d$–$q)_{2\theta}$ currents due to the offset where the magnitude is proportional to the offset error. Nevertheless, since both components in (27) and (28) are periodic errors, produce negligible dc offset component averaging over an interval with a period $T_s/2$ in the second-order reference frame.

An experimental evolution is provided in this part to verify the immunity of fault diagnosis technique against the current sensor measurement errors. The 5% offset on a-phase current and -5% on c-phase current are selected for result comparison. As seen in Fig. 22, remarkable oscillations appear in d–q currents due to current offset. However, in spite of the current measurements errors, the waveforms of the $\overline{I}^{\,\mathrm{pu}}_{d(2\theta)}$ and $\overline{I}^{\,\mathrm{pu}}_{q(2\theta)}$ in Fig. 22 allow robust verification of fault detection. Clearly, diagnostic signals do not show observable variations. Comparing the detection method developed in [19] it is clear that, the fault diagnostic variables have a very similar behavior when there is no current measurement error, while in [19] a small current offset can induce a large error on fault detection signals which, might result in false alarms [23].

V. COMPARISON OF PROPOSED AND DIFFERENT FAULT DIAGNOSIS METHODS

In this section, some important indices are selected to investigate the strengths and limitations of the different fault diagnostic techniques. The results of this comparative study are shown in Table V. The detection time, robustness (speed transients, motor start-up, and load disturbance), sensitivity to motor parameters, cost, and implementation complexity, are taken into consideration. By comparing the various indices as a whole, it is found that the proposed scheme, presents highly efficient performance while the other approaches have one or more deficiencies.

VI. CONCLUSION

In order to prevent damage to the motor drive system, the open-phase faults need to be immediately and effectively detected. This paper offers a novel low-cost fault detection technique for three-phase machines using SORP transformation. It ensures trustable fault alarms at different operating conditions without additional hardware requirement. According to experimental evaluations, the proposed scheme presents robust behaviour over the entire speed range and different load conditions. Moreover, it presents high robustness against the transients and current measurement error. Due to faster fault detection in the second-order d–q frame, less computation amount and memory storage are required in comparison to rms based methods. Finally, the developed signal processing strategy has a simpler structure than conventional methods which is important for industrial control applications.

REFERENCES

[1] Tian-Hua Liu, Jen-Ren Fu, and T. A. Lipo, "A strategy for improving reliability of field-oriented controlled induction motor drives," *IEEE Trans. Industry Appl.*, vol. 29, no. 5, pp. 910–918, Sep./Oct. 1993.
[2] H. Henao *et al.*, "Trends in fault diagnosis for electrical machines: A review of diagnostic techniques," *IEEE Ind. Electron. Mag.*, vol. 8, no. 2, pp. 31–42, Jun. 2014.
[3] Y. Song and B. Wang, "Analysis and experimental verification of a fault-tolerant HEV powertrain," *IEEE Trans. Power Electron.*, vol. 28, no. 12, pp. 5854–5864, Dec. 2013.
[4] B. A. Welchko, T. A. Lipo, T. M. Jahns, and S. E. Schulz, "Fault tolerant three-phase AC motor drive topologies: A comparison of features, cost, and limitations," *IEEE Trans. Power Electron.*, vol. 19, no. 4, pp. 1108–1116, Jul. 2004.
[5] B. Mirafzal, "Survey of fault-tolerance techniques for three-phase voltage source inverters," *IEEE Trans. Ind. Electron.*, vol. 61, no. 10, pp. 5192–5202, Oct. 2014.
[6] Y. Fan, W. Zhu, X. Zhang, M. Cheng, and K. T. Chau, "Research on a single phase-loss fault-tolerant control strategy for a new flux-modulated permanent-magnet compact in-wheel motor," in *IEEE Trans. Energy Convers.*, vol. 31, no. 2, pp. 658–666, Jun. 2016.
[7] E. Ribeiro, A. J. M. Cardoso, and C. Boccaletti, "Open-circuit fault diagnosis in interleaved DC–DC converters," *IEEE Trans. Power Electron.*, vol. 29, no. 6, pp. 3091–3102, Jun. 2014.
[8] P. Nuutinen, P. Peltoniemi, and P. Silventoinen, "Short-circuit protection in a converter-fed low-voltage distribution network," *IEEE Trans. Power Electron.*, vol. 28, no. 4, pp. 1587–1597, Apr. 2013.

[9] U. Choi, H. Jeong, K. Lee, and F. Blaabjerg, "Method for detecting an open-switch fault in a grid-connected NPC inverter system," *IEEE Trans. Power Electron.*, vol. 27, no. 6, pp. 2726–2739, Jun. 2012.
[10] J.-C. Urresty, J.-R. Riba, and L. Romeral, "Application of the zero-sequence voltage component to detect stator winding inter-turn faults in PMSMs," *Elect. Power Syst. Res*., vol. 89, pp. 38–44, Aug. 2012.
[11] C. Gan, J. Wu, S. Yang, Y. Hu, W. Cao, and J. Si, "Fault diagnosis scheme for open-circuit faults in switched reluctance motor drives using fast Fourier transform algorithm with bus current detection," *IET Power Electron.*, vol. 9, no. 1, pp. 20–30, 2016.
[12] B. Cai, Y. Zhao, H. Liu, and M. Xie, "A data-driven fault diagnosis methodology in three-phase inverters for PMSM drive systems," *IEEE Trans. Power Electron.*, vol. 32, no. 7, pp. 5590–5600, Jul. 2017.
[13] A. Sapena-Bano, M. Pineda-Sanchez, R. Puche-Panadero, J. Martinez-Roman, and D. Matic, "Fault diagnosis of rotating electrical machines in transient regime using a single stator current's FFT," *IEEE Trans. Instrum. Meas.*, vol. 64, no. 11, pp. 3137–3146, Nov. 2015.
[14] J. O. Estima and A. J. Marques Cardoso, "A new approach for real-time multiple open-circuit fault diagnosis in voltage-source inverters," *IEEE Trans. Industry Appl.*, vol. 47, no. 6, pp. 2487–2494, Nov./Dec. 2011.
[15] D. Diallo, M. E. H. Benbouzid, D. Hamad, and X. Pierre, "Fault detection and diagnosis in an induction Machine drive: a pattern recognition approach based on Concordia stator mean current vector," *IEEE Trans. Energy Convers.*, vol. 20, no. 3, pp. 512–519, Sep. 2005.
[16] N. M. A. Freire, J. O. Estima, and A. J. Marques Cardoso, "Open-circuit fault diagnosis in PMSG drives for wind turbine applications," *IEEE Trans. Ind. Electron.*, vol. 60, no. 9, pp. 3957–3967, Sep. 2013.
[17] J. O. Estima and A. J. Marques Cardoso, "A new algorithm for real-time multiple open-circuit fault diagnosis in voltage-fed PWM motor drives by the reference current errors," *IEEE Trans. Ind. Electron.*, vol. 60, no. 8, pp. 3496–3505, Aug. 2013.
[18] H. Yan, Y. Xu, J. Zou, Y. Fang, and F. Cai, "A novel open-circuit fault diagnosis method for voltage source inverters with a single current sensor," *IEEE Trans. Power Electron.*, vol. 33, no. 10, pp. 8775–8786, Oct. 2018.
[19] S. S. Kuruppu and N. A. Kulatunga, "D-Q current signature-based faulted phase localization for SM-PMAC machine drives," *IEEE Trans. Ind. Electron.*, vol. 62, no. 1, pp. 113–121, Jan. 2015.
[20] J. Hang, J. Zhang, M. Cheng, and S. Ding, "Detection and discrimination of open-phase fault in permanent magnet synchronous motor drive system," *IEEE Trans. Power Electron.*, vol. 31, no. 7, pp. 4697–4709, Jul. 2016.
[21] J. Hang, J. Zhang, M. Cheng, and J. Huang, "Online interturn fault diagnosis of permanent magnet synchronous machine using zero-sequence components," *IEEE Trans. Power Electron.*, vol. 30, no. 12, pp. 6731–6741, Dec. 2015.
[22] S. Yang, G. Chen, and D. Jian, "On-line stator open-phase fault detection and tolerant control for permanent magnet machines using the neutral point voltage," *IEEE Access*, vol. 5, pp. 1073–1082, 2017.
[23] S. Yang, Y. Hsu, P. Chou, G. Chen, and D. Jian, "Online open-phase fault detection for permanent magnet machines with low fault harmonic magnitudes," *IEEE Trans. Ind. Electron.*, vol. 65, no. 5, pp. 4039–4050, May 2018.
[24] S. Jung, J. Park, H. Kim, K. Cho, and M. Youn, "An MRAS-based diagnosis of open-circuit fault in PWM voltage-source inverters for PM synchronous motor drive systems," *IEEE Trans. Power Electron.*, vol. 28, no. 5, pp. 2514–2526, May 2013.
[25] A. Kontarček, P. Bajec, M. Nemec, V. Ambrožič, and D. Nedeljković, "Cost-effective three-phase PMSM drive tolerant to open-phase fault," *IEEE Trans. Ind. Electron.*, vol. 62, no. 11, pp. 6708–6718, Nov. 2015.
[26] J. Zhang, J. Zhao, D. Zhou, and C. Huang, "High-performance fault diagnosis in PWM voltage-source inverters for vector-controlled induction motor drives," *IEEE Trans. Power Electron.*, vol. 29, no. 11, pp. 6087–6099, Nov. 2014.
[27] F. Wu and J. Zhao, "A real-time multiple open-circuit fault diagnosis method in voltage-source-inverter fed vector controlled drives," *IEEE Trans. Power Electron.*, vol. 31, no. 2, pp. 1425–1437, Feb. 2016.
[28] L. M. A. Caseiro and A. M. S. Mendes, "Real-time IGBT open-circuit fault diagnosis in three-level neutral-point-clamped voltage-source rectifiers based on instant voltage error," *IEEE Trans. Ind. Electron.*, vol. 62, no. 3, pp. 1669–1678, Mar. 2015.
[29] T. Kamel, Y. Biletskiy, and L. Chang, "Real-time diagnosis for open-circuited and unbalance faults in electronic converters connected to residential wind systems," *IEEE Trans. Ind. Electron.*, vol. 63, no. 3, pp. 1781–1792, Mar. 2016.
[30] Z. Gao, C. Cecati, and S. X. Ding, "A survey of fault diagnosis and fault-tolerant techniques—part I: Fault diagnosis with model-based and signal-based approaches," *IEEE Trans. Ind. Electron.*, vol. 62, no. 6, pp. 3757–3767, Jun. 2015.
[31] Z. Gao, C. Cecati, and S. X. Ding, "A survey of fault diagnosis and fault-tolerant techniques—part II: Fault diagnosis with knowledge-based and hybrid/active approaches," *IEEE Trans. Ind. Electron.*, vol. 62, no. 6, pp. 3768–3774, Jun. 2015.
[32] J. F. Martins, V. Ferno Pires, and A. J. Pires, "Unsupervised neural-network-based algorithm for an on-line diagnosis of three-phase induction motor stator fault," *IEEE Trans. Ind. Electron.*, vol. 54, no. 1, pp. 259–264, Feb. 2007.
[33] M. S. Ballal, Z. J. Khan, H. M. Suryawanshi, and R. L. Sonolikar, "Adaptive neural fuzzy inference system for the detection of inter-turn insulation and bearing wear faults in induction motor," *IEEE Trans. Ind. Electron.*, vol. 54, no. 1, pp. 250–258, Feb. 2007.
[34] F. Zidani, D. Diallo, M. E. H. Benbouzid, and R. Nait-Said, "A fuzzy-based approach for the diagnosis of fault modes in a voltage-fed PWM inverter induction motor drive," *IEEE Trans. Ind. Electron.*, vol. 55, no. 2, pp. 586–593, Feb. 2008.
[35] M. J. Duran, I. Gonzalez-Prieto, N. Rios-Garcia, and F. Barrero, "A simple, fast, and robust open-phase fault detection technique for six-phase induction motor drives," *IEEE Trans. Power Electron.*, vol. 33, no. 1, pp. 547–557, Jan. 2018.
[36] J. A. Santisteban and R. M. Stephan, "Vector control methods for induction machines: An overview," *IEEE Trans. Educ.*, vol. 44, no. 2, pp. 170–175, May 2001.
[37] W. Im, J. Kim, D. Lee, and K. Lee, "Diagnosis and fault-tolerant control of three-phase AC–DC PWM converter systems," *IEEE Trans. Industry Appl.*, vol. 49, no. 4, pp. 1539–1547, Jul./Aug. 2013.
[38] H.-S. Jung, S.-H. Hwang, J.-M. Kim, C.-U. Kim, and C. Choi, "Diminution of current-measurement error for vector-controlled AC motor drives," *IEEE Trans. Industry Appl.*, vol. 42, no. 5, pp. 1249–1256, Sep./Oct. 2006

Ali Hajary was born in Ahvaz, Iran, in 1987. He received the B.S. and M.Sc. degrees from Shahid Chamran University of Ahvaz, Iran, in 2009 and 2015, respectively. He is currently working toward the Ph.D. degree in the Department of Electric Drive Laboratory of the Faculty of Engineering. His research interests include fault-tolerant variable-speed ac motor drives, and fault diagnosis and multiphase machines.

Reza Kianinezhad was born in Ahvaz, Iran, in 1963. He received the B.Sc. degree in electrical engineering from Shahid Chamran University of Ahvaz, Iran, in 1988, the M.Sc. degree in electrical power engineering from Tarbiyat Modares University, Tehran, Iran, in 1995, and the Ph.D. degree from the University of Picardie Jules-Verne, Amiens, France, in 2006.

He worked for seven years in the Electrical Engineering Department, Shahid Chamran University, as a Lecturer, where he is currently an Associate Professor. His research interests include modeling and control of multiphase induction machines.

S.Gh Seifossadat was born in Ahvaz, Iran, on August 28, 1963. He received the B.Sc. degree in electrical engineering from the Iran University of Science and Technology (IUST), Tehran, Iran, in 1989, and the M.Sc. degree in electrical engineering from the Ferdosi University of Mashhad, Mashhad, Iran, in 1992, and the Ph.D. degree from IUST in 2006. Currently, he is a Professor with the Department of Electrical Engineering, Shahid Chamran University of Ahvaz, Iran, where he has been since 1992. His research interests include power system protection and power quality.

S.S Mortazavi was born in Behbahan, Iran, on Feb, 8, 1964 and received B.Sc. and M.Sc. degrees in electrical engineering from Ferdowsi University, Mashad, Iran in 1989 and 1992, respectively. He received the Ph.D. degree in electrical engineering from Indian Institute of Technology Delhi (IIT)-Delhi, India, in January 1999. He is currently a Professor with the Department of Electrical Engineering, Shahid Chamran University of Ahvaz, Iran, where he has been since 1999. His research interests include intelligent control and power system control and operation.

Alireza Saffarian was born in 1981 in Ahvaz, Iran. He received the B.Sc and M.Sc. degrees in electrical engineering from the Amirkabir University of Technology, Tehran, Iran, in 2003 and 2005, respectively, and the Ph.D. degree from University of Tehran, Tehran, Iran, in 2011. Currently, he is an Assistant Professor with the Department of Electrical Engineering, Shahid Chamran University of Ahvaz, Iran. His research interests include power system protection, power system stability, and power quality assessment.